Susceptibility perturbation MRI (SPI) maps tumor infiltration into mesorectal lymph nodes

Inês Santiago[a,b,c], João Santinha[d], Andrada Ianus[a,e], Antonio Galzerano[f], Rita Theias[g], Joana Maia[h], Maria J. Barata[b], Nuno Loução[i], Bruno Costa-Silva[h], Antonio Beltran[f], Celso Matos[b], Noam Shemesh[a*]

a Neuroplasticity and Neural Activity Lab, Champalimaud Research, Champalimaud Centre for the Unknown, Av. Brasília, 1400-038, Lisbon, Portugal
b Radiology Department, Champalimaud Centre for the Unknown, Av. Brasília, 1400-038, Lisbon, Portugal
c Nova Medical School, Campo Mártires da Pátria, 130, 1169-056 Lisbon, Portugal
d Computational Clinical Imaging Group, Champalimaud Centre for the Unknown, Av. Brasília, 1400-038, Lisbon, Portugal
e Centre for Medical Imaging Computing, Department of Computer Science, University College London, Malet Place, London WC1E7JE, United Kingdom
f Pathology Department, Champalimaud Centre for the Unknown, Av. Brasília, 1400-038, Lisbon, Portugal
g Pathology Department, Hospital Fernando Fonseca, EPE, IC19 2720-276 Amadora, Portugal
h Systems Oncology Lab, Champalimaud Research, Champalimaud Centre for the Unknown, Av. Brasília, 1400-038, Lisbon, Portugal
i Philips Healthcare Iberia, Maria de Portugal 1. 28050, Madrid, Spain

*****Corresponding author: Dr. Noam Shemesh, Champalimaud Research, Champalimaud Centre for the Unknown, Av. Brasilia 1400-038, Lisbon, Portugal.
E-mail: noam.shemesh@neuro.fchampalimaud.org.
Phone number: +351 210 480 000 ext. #4467.

Running Title: Mapping tumor in mesorectal lymph nodes using SPI

Conflicts of interest: Nuno Loução is an employee of Philips Healthcare. All other authors declare no potential conflicts of interest relevant to the content of this paper.

ABSTRACT

Noninvasive characterization of lymph node involvement in cancer is an enduring onerous challenge. In rectal cancer, pathologic lymph node status constitutes the most important determinant of local recurrence and overall survival and patients with involved lymph nodes may benefit from pre-operative chemo and/or radiation therapy. However, knowledge of lymph node status before surgery is currently hampered by limited imaging accuracy. Here, we introduce Susceptibility-Perturbation MRI (SPI) as a novel source of contrast to map malignant infiltration into mesorectal lymph nodes. SPI involves multigradient echo (MGE) signal decays presenting a non-monoexponential nature, which we show is sensitive to the underlying microstructure via susceptibility perturbations. Using numerical simulations, we predicted that the large cell morphology and the high cellularity of tumor within affected mesorectal lymph nodes would induce signature SPI decays. We validated this prediction in mesorectal lymph nodes excised from total mesorectal excision specimens of rectal cancer patients using ultrahigh field (16.4 T) MRI. SPI signals distinguished benign from malignant nodal tissue, both qualitatively and quantitatively, and our histologic analyses confirmed cellularity and cell size were the likely underlying sources for the differences observed. SPI was then adapted to a clinical 1.5 T equipment, added to patient´s staging protocol and compared with conventional assessment by two expert radiologists. Non-monoexponential decays, similar to those observed in the ex-vivo study were demonstrated, and SPI classified lymph nodes more accurately than standard high-resolution T_2-weighted imaging assessment. These findings suggest this simple – yet extremely informative – method can improve rectal cancer patient selection for neoadjuvant therapy.

PRECIS

Findings introduce an MRI method tailored to detect magnetic susceptibility perturbations induced by subtle alterations in tissue microstructure.

KEYWORDS

Rectal cancer; Lymph nodes; SPI; Multi-gradient echo; Multi-exponential model.

1. INTRODUCTION

In rectal cancer, pathologic lymph node status of the mesorectum constitutes the most important determinant of local recurrence and overall survival (1). Standard assessment is based on hematoxylin and eosin (H&E) stained slides (1), which can identify malignancy based on the contrast between small, roughly round and loosely-packed leucocytes and much larger, goblet-shaped, tightly packed malignant epithelial cells. This information becomes available only with radical surgery; however, neoadjuvant chemoradiation therapy is associated with lower incidences of local relapse in patients with high risk features, including lymph node positivity, when compared to postoperative regimens (6% vs 13% at 5-years) (2). This justifies the need for accurate pre-operative non-invasive imaging-based lymph node characterization.

Magnetic Resonance Imaging (MRI) is safe, noninvasive and benefits from extremely versatile physics giving rise to a multitude of contrast mechanisms which, in turn, can highlight different aspects of biological tissue. One of the most important sources of MRI contrast is dephasing in the transverse plane, typically characterized by a time constant T_2 – the spin-spin relaxation. T_2 is affected by alkali cation composition and tissue microstructure and has been shown to be capable of differentiating between normal tissue and malignant tumors since the very beginning of MRI (3). Indeed, T_2-weighted MRI (T2-WI) remains the gold standard for pelvic staging in rectal cancer, but it is unfortunately inaccurate with respect to lymph node involvement (4,5). However, more generally, the MRI signal can be sensitized to transverse dephasing induced by local field variations arising from susceptibility distributions. In this case, the transverse relaxation constant is described by $1/T_2^* = 1/T_2 + 1/T_2'$, where T_2' characterizes the additional source of dephasing (6). Divalent calcium or trivalent iron cations, as well as tissue oxygenation, are important sources of susceptibility-induced local field variations and their characterization is routinely performed using T_2^*-sensitive sequences such as gradient-echo MRI. Interestingly, gradient echo MRI has been also performed in the context of lymph node characterization. A study on dissected axillary lymph nodes at 7T demonstrated that the T_2* of metastatic lymph nodes was distinct from that of benign nodes (7). A subsequent similar study performed in-vivo at 3T reached similar conclusions (8), though the mechanism underlying these T_2* variations remains to be elucidated.

T_2* is a “generic” parameter which can only be accurately estimated in the (approximately) linear, low echo-time regime of a multigradient echo (MGE) signal decay. This generic linear decay with the log of the signal decay is quite “featureless”: dramatic changes in susceptibility would be required to induce a significant variation in the T_2*. However, the underlying physics (9-11) suggest that in most realistic scenarios, magnetic fields would be distributed according to susceptibility-driven perturbations leading to non-exponential (9) and even non-monotonic (10) signals, which potentially reflect microstructural tissue properties. Curiously, the vast majority of studies assumed that it is sufficient to measure the “linear” component at short echo times, and only very few studies ventured towards measuring the full MGE decay up to longer TEs, which could reflect the underlying susceptibility perturbations much better. Indeed, the few studies that have measured the full MGE decay have discovered that much more detailed information could be potentially extracted. For example, Chen et al reconstructed the shape and orientation of white matter substructures and their arrangement relative to one another in humans at 3T from multi-exponential MGE decays measured up to long TEs (9). Nunes et al probed ex-vivo rat spinal cords at 16.4 T and found non-exponential, and non-monotonic MGE decays, which were simply modeled by two compartments (axons + extra-axonal space) leading to axon density quantification (10). Qian et al scanned tibial cartilage explants at 3T and classified different types of MGE decays, where the short T_2* component differentiated diseased from healthy cartilage successfully, while the monoexponential T_2* model did not (11).

Normal lymph nodes are composed of a relatively uniform and loose distribution of small lymphocytes. By contrast, malignancy is characterized by the presence of tightly-packed large malignant epithelial cells. Since susceptibility-driven magnetic field distributions depend on the underlying compartment sizes, we hypothesized that MGE signals could reflect these intrinsic susceptibility disturbances and distinguish the infiltrated from normal nodal tissue. We term this long-echo MGE approach Susceptibility Perturbation MR Imaging (SPI) since it probes susceptibility perturbations due to microstructure. We tested SPI using numerical simulations and ultrahigh magnetic field MRI experiments (16.4 T) in mesorectal lymph nodes extracted from the surgical specimens of rectal cancer patients. We elucidated the mechanisms underlying the emerging SPI contrasts using quantitative histologic analysis. Finally, we translated the experiment to an in-vivo 1.5 T scanner, upon patient staging, for clinical applicability assessment, in which the SPI contrast was again observed. Our findings indicate that SPI is superior to the current standard methodology for lymph node involvement characterization in-vivo.

2. MATERIALS AND METHODS

2.1 Simulations

Numerical simulations were performed to predict whether changes in cellularity could affect MGE decays. To this end, we simulated susceptibility-driven magnetic field distribution maps arising from randomly packed spheres with different distributions of cell sizes and intracellular volume fractions. The magnetic field distribution for an individual sphere of radius R located at position (x_0,y_0,z_0) in a 3D mesh (x,y,z) is given in equation 1 (12,13):

$$\boldsymbol{Equation\ 1}: \Delta B^{sph}(x,y,z) = B_0 \begin{cases} \frac{1}{3}\chi R^3 \frac{(2(z-z_0)^2-(x-x_0)^2-(y-y_0)^2)}{((z-z_0)^2+(x-x_0)^2+(y-y_0)^2)^{5/2}} & \text{outside the sphere} \\ 0 & \text{inside the sphere} \end{cases}$$

Following others (14), in this study we used a susceptibility difference of $\chi = 6\cdot10^{-7}$(14) in all simulations.

Guided by our histology assessment, we designed two tissue configurations corresponding to the microstructure of benign and malignant tissue, respectively. The benign tissue configuration employed a distribution of spherical radii corresponding to a lognormal distribution of areas with mean of 12.2 μm^2 and standard deviation of 6.1 μm^2 packed in a 50×50×50 μm^3 cube with intracellular volume fraction of 24%. For the malignant tissue configuration, we used a similar lognormal distribution, but now with a mean of 92.7 μm^2 and standard deviation of 49.8 μm^2, packed in a 50×50×50 μm^3 volume with 61% intracellular volume fraction. Once the configurations were set, the field map $\Delta B(x,y,z)$ was calculated as the sum over the contributions of all individual spheres within each substrate.

Once the field maps were produced for every substrate, the MGE signal in the simulated “voxel” could be calculated by simply summing across the entire “voxel”, as represented in equation 2:

$$\boldsymbol{Equation\ 2}: S_{MGE}(TE) = \iiint_{x,y,z} \exp(i\gamma\Delta B(x,y,z)\cdot TE)$$

2.2 Ultrahigh field SPI of ex-vivo lymph nodes

Institutional setting and lymph node harvesting

This study was approved by the institutional ethics committee and written informed consent was obtained from twenty-five consecutive rectal cancer patients that agreed to participate in the study. Six of these patients were excluded because they underwent neoadjuvant therapy and another three were excluded because they chose to be operated in a different institution. Sixteen patients underwent surgery without neoadjuvant therapy and their total mesorectal excision specimens were immersed in a 4% formaldehyde solution for 72 h. During macroscopic specimen processing, the otherwise discarded halves of lymph nodes present in more than 1 cut slice, approximately 5 mm in thickness, were collected and labeled to match the halves sent for pathologic staging, which was performed by a gastrointestinal pathologist (8 years of experience), according to the cancer protocol defined by the College of American Pathologists (https://www.cap.org/protocols-and-guidelines/cancer-reporting-tools/cancer-protocol-templates). Pathologic staging resulted in the exclusion of an additional 5 patients with node negative disease. A total of 11 patients were included (mean age 61.6 years, 5 males).

Acquisition protocol at 16.4T

Retrieved lymph node “halves” from each patient were grouped in benign/malignant pairs based on the information from pathologic staging, preferably originating from the same histopathologic block and with a similar size. Prior to scanning, the nodes were washed with a 1% phosphate buffered saline solution for 24 h and then immersed in Flourinert® within a 10 mm NMR tube.

The preclinical MRI images were acquired at 37ºC on a 16.4T Bruker Aeon Ascend scanner (Bruker Biospin, Karlruhe, Germany) using a Micro5 probe with a gradient system capable of producing up to 3000 mT/m in all directions. A MGE acquisition was performed with the following parameters: 50 echo times starting at 1.6 ms with 1.4 ms interval, repetition time of 1500 ms, flip angle of 50º, slice thickness of 0.3 mm, a field-of-view of 12x12 mm^2 and matrix size of 120x120, leading to an in-plane resolution of 0.1x0.1 mm^2. The acquisition bandwidth was set to 125 kHz and 25 signal averages were acquired, leading to a total scan time of 1h12m per node.

Histopathologic analysis for validation of the MRI findings

The scanned “halves” of lymph nodes were embedded in paraffin and 6 consecutive 4 µm slices were cut every 50 µm using a Leica RM2245 microtome (Leica Biosystems. Newcastle, United Kingdom) in a plane parallel to the cut surface of the node, similarly to the MRI acquisition. One slice per interval was stained with hematoxylin-eosin (H&E) and analyzed by the gastrointestinal pathologist (8 years of experience) using a Zeiss Axio Lab A1, (Carl Zeiss Microscopy GmbH Germany) with a 40x amplification. The analysis of the scanned “halves” resulted in reclassification of 3 previously-defined benign nodes as malignant. Given they all originated from patients already classified as N+, this did not impact patient management. In total, we scanned and analyzed 29 benign and 35 malignant lymph nodes.

In four representative lymph nodes, the remaining 4 µm slices were used for additional characterization: Pearls coloration (Iron Staining Kit. Ventana Medical Systems, Inc. Tucson, Arizona, USA) was used to quantify iron-containing MR-field-disturbing particles; an antibody against CD45 (CD45, QBEnd/10, Leica Biosystems. Newcastle. United Kingdom) was used to mark leucocytes; and multi-cytokeratin AE1/AE3 (Leica Biosystems. Newcastle. United Kingdom) was used to mark adenocarcinoma cells.

MR image analysis

Multi-gradient echo datasets were denoised in Matlab® (Mathworks, MA, USA) using Marchenko-Pastur principle component analysis (15) with a window size of 7x7. Benign and malignant histology-matched regions-of-interest (ROIs) were defined by a dedicated radiologist (10 years of experience). Three ROIs were placed per node, in the most representative slice; in malignant nodes, malignant areas were selected based on MR-histology co-registration (see subtopic below). The mean signal value per node was computed for each TE. Although SPI in principle leads to a field distribution, we here simplified the complex expressions by assuming that one, two or three components would be sufficient to describe the signal decay. In the multiexponential models, one compartment was arbitrarily assumed to be on resonance while the others exhibited a frequency shift. The signal expressions for 1-compartment, 2-compartment and 3-compartment models are given in equations 3, 4 and 5, respectively.

$$\boldsymbol{Equation\ 3}: S_{1c} = S_0 \exp(-TE/T_2^*).$$

$$\boldsymbol{Equation\ 4}: S_{2c} = S_0 \left| f^a \exp\left(-\frac{TE}{T_2^{*a}}\right) + (1-f^a)\exp\left(-TE\left(\frac{1}{T_2^{*b}} + i\Delta\omega^b\right)\right)\right|$$

$$\boldsymbol{Equation\ 5}: S_{3c} = S_0 \left| f^a \exp\left(-\frac{TE}{T_2^{*a}}\right) + f^b \exp\left(-TE\left(\frac{1}{T_2^{*b}} + i\Delta\omega^b\right)\right) + (1-f^a-f^b)\exp\left(-TE\left(\frac{1}{T_2^{*c}} + i\Delta\omega^c\right)\right)\right|$$

where TE is the echo time, S_0 is the signal at TE = 0 and $T_2{*}^i$ is the relaxation time of compartment i which has a volume fraction f^i and frequency shift $\Delta\omega^i$.

Voxel-by-voxel fitting of the signal models above to the experimental data was performed for the whole dataset.

MR-pathology co-registration

Histology H&E slides were scanned at a Philips ultrafast scanner 1.6 (Philips Healthcare, Andover, United States), stacked into a volume and registered to MGE images using SimpleElastix (16). For the stacking step, a 2D-rigid pairwise registration was performed, in which a set of 3 to 6 corresponding control points were defined on each pair of histology images and the translations and rotations were estimated using adaptive stochastic gradient descent, minimizing both the advanced mattes mutual information and the corresponding points Euclidean distance metric. The registration of a given stack to the MGE images utilized a 3D-rigid registration scheme with 6 to 12 corresponding control points defined in the two volumes and optimized using adaptive stochastic gradient descent that minimized both the advanced mattes mutual information and the corresponding points Euclidean distance metric.

Histology quantification

With the purpose of understanding the parametric differences encountered between benign and malignant lymph node tissue, we analyzed histology H&E slides and obtained measurements of cellularity and cell size. To ensure histology measurements were as representative as possible, we first selected the single H&E slide from the volume stack that best matched the MGE image in which the ROIs were placed. The selection was based on specific contour and inner landmarks that could be found in both MGE and scanned H&E images at low magnification (0.03x). Then, from each MGE-ROI-matching histology area and at higher magnification (0.42x), 3 random 50x50 µm fields were selected and a cell detection tool (QuPath®, Belfast, UK) was employed to quantify cell number, nucleus area and cell area.

Statistical analysis

Signal decay models were compared based on Bayesian Information Criterion (BIC), which describes the goodness of fit, penalizing for increasing number in model parameters, as represented in equation 6.

$$\textbf{\textit{Equation 6:}}\, BIC = \ln(N)\,k - 2\ln(\hat{L})$$

where N is the number of data points, k is the number of model parameters (1 for monoexponential decay, 4 for biexponential decay and 7 for triexponential decay) and $\ln(\hat{L})$ is the maximum value of the log likelihood function of the model. Specifically, $\ln(\hat{L})$ is the negative of the sum of squared differences between the model prediction and the measured data, which was also used as objective function for non-linear fitting of the models.

For all parameters extracted from the models, comparison between benign and malignant was based on the Mann-Whitney U test, given data was not normally distributed. An $\alpha<0.05$ was considered as the statistical significance threshold.

Spearman´s rank correlation coefficient was the test used to establish the statistical dependence between the rankings of model parameters and histology metrics. Bonferroni correction was employed to account for multiple comparisons.

2.3 Translation of SPI to the clinic, in-vivo at 1.5 T

This study was also approved by the institution´s ethics committee and written informed consent was obtained. In 8 participating patients, Butylscopolamine 20 mg was administered intravenously to minimize bowel movement and a stereotactic body radiation therapy pressure belt with manual pump insuflated to 20-40 mmHg (Orfit Industries, Wijnegem, Belgium) was used to minimize respiratory movement artifacts. A MGE sequence with the following parameters was added to the staging pelvic MRI, which was performed on a 1.5 T clinical scanner (Ingenia, Philips Healthcare®, Andover, United States): 32 TEs were acquired starting at 2.37 ms with a 2.37 ms interval; repetition time of 1971 ms; flip angle of 55º; slice thickness of 4 mm; field of view of 20x20 cm^2, matrix size of 480x480, bandwidth of 431Hz and 2 signal averages, leading to an in-plane resolution of 0.42x0.42mm^2 and a total acquisition time of 11m19s.

Whole-node ROIs were defined for all visible lymph nodes on the single slice with the largest surface by a general radiologist (11 years of experience). Mapping during specimen processing allowed 36 benign and 27 malignant lymph nodes originating from the 6 patients subsequently selected for surgery without preoperative therapy at multidisciplinary team meeting (mean age, 61.7 years; 4 males) to be matched to MGE images (2 patients were excluded because they underwent neoadjuvant therapy). Models were fitted to the median magnitude signal of each lymph node, given the reduced number of voxels per node and deviation from normality of the distribution of signal intensities. Two radiologists dedicated to gastrointestinal and abdominal imaging (10 and 13 years of experience), blinded to pathology results, independently performed a node-by-node classification in the corresponding axial, coronal and sagittal high-resolution T_2-WI in accordance with the ESGAR 2016 recommendations for nodal staging (17). Reliability of the T_2-WI-based analysis was estimated using the intraclass correlation coefficient (<0.40 = poor; 0.40 to 0.59 = Fair; 0.60 to 0.74 = good; 0.75 to 1.00 = excellent). The SPI and T_2-WI analysis and their combination were compared using logistic regression. The statistical significance of the differences between the corresponding areas under the ROC curves (AuROC) were tested using the De Long Test.

3. RESULTS

3.1 Simulations

Our first goal was to simulate whether microstructural changes induced by the infiltration of malignant cells into lymph nodes would produce significant perturbations to magnetic field distributions. Figures 1a and 1b simulate the spatial distribution of magnetic fields in the “benign” substrate (small spheres, low volume fraction) and “malignant” substrate (infiltration of large spheres, with large volume fraction), respectively. Importantly, these field distributions give rise to a non-monoexponential MGE signal decay (Figure 1c, note the signal oscillation), which is more evident perhaps in the logarithmic plot (Fig. 1d). Perhaps even more importantly, these simulations predict a slower decay for small spheres with low volume fraction (benign tissue) and a faster decay for larger spheres with high volume fraction (malignant tissue), suggesting that T_2* measurements could inform about tissue microstructure.

3.2 Ultrahigh field SPI of ex-vivo lymph nodes

To test the validity of the above predictions and investigate whether SPI could distinguish between normal nodal tissue and nodal tissue infiltrated by malignancy, we performed ultrahigh field ex-vivo experiments with very high spatial and TE resolution on 29 benign and 35 malignant lymph nodes (64 lymph nodes in total). Figure 2a shows that the normalised MGE signal decay for both benign and malignant tissue is indeed non-monoexponential. TE-dependent differences between the signal decay of the different groups are already apparent from the raw data (Fig. 2a). A BIC analysis for model selection (e.g., between Eq. 1, 2 and 3) reveals that the 2-compartment model represents the data better than a 1- or 3-compartment model in the vast majority of voxels (Figure 2b).

Figure 2a also reveals clear and dramatically different SPI decays for benign and malignant tissue: while the former decays slowly, the latter decays much more rapidly.

Given that the 2-compartment model was selected from the BIC values, further analysis was focused on this model. The median values of T_2*a were significantly shorter in malignant tissue, by a factor of ~2 (malignant = 15.05ms; benign = 29.59 ms; $p = 1 \times 10^{-4}$), as were the median values of T_2*b, by a factor of ~2.3 (malignant = 10.71 ms; Benign = 24.64 ms; $p = 1 \times 10^{-4}$). In addition, in absolute value, the median frequency shift $\Delta\Omega$ was significantly larger in malignant tissue, by a factor of ~1.6 (malignant = -0.08 rad; benign = -0.05 rad; $p = 8 \times 10^{-4}$). The fraction of the first component did not exhibit a significant difference between tissues (malignant = 0.62; benign = 0.66; p = 0.097). Figure 3 depicts these measurement differences as boxplots.

We next turn to the histological analyses, where striking microstructural differences were found. In benign nodal tissue, the predominant cell type – lymphocyte - is small, round, and practically devoid of visible cytoplasm. Adenocarcinoma cells, on the other hand, are cytoplasm rich and much larger. When quantified, we found that cell size, both in terms of nuclear area (benign: $\bar{x} = 12.36$ and $\sigma_{\bar{x}} = 0.99\ \mu m^2$; malignant: $\bar{x} = 23.77$ and $\sigma_{\bar{x}} = 4.16\ \mu m^2$; $p = 5.99 \times 10^{-7}$) and total cell area (benign: $\bar{x} = 12.36$ and $\sigma_{\bar{x}} = 0.99\ \mu m^2$; malignant: $\bar{x} = 104.34$ and $\sigma_{\bar{x}} = 23.53\ \mu m^2$; $p = 2.23 \times 10^{-8}$), was higher in malignant tissue while the mean number of cells per surface area was much lower (benign: $\bar{x} = 19.91 \times 10^{-3}$ and $\sigma_{\bar{x}} = 2.69 \times 10^{-3}$ cells/μm^2; malignant: $\bar{x} = 6.62 \times 10^{-3}$ and $\sigma_{\bar{x}} = 3.73 \times 10^{-3}$ cells/μm^2; $p = 5 \times 10^{-3}$). We also attempted to directly correlate SPI parameters with the cellularity and cell size by registering MR images with the histological slices (Figure 4a). We found significant correlations between T_2*b, our best-performing parameter, and both number of cells per surface area ($\rho = 0.52$, considered moderate; $p = 9.18 \times 10^{-6}$) and mean nuclear area ($\rho = -0.56$, considered moderate; $p = 1.14 \times 10^{-6}$) (Figure 4b).

We also noted a variety of infiltration patterns in malignant lymph nodes, namely cellular areas (those constituted by tightly packed malignant cells), areas of necrosis and areas of tumor-induced desmoplasia. These patterns tend to coexist in malignant lymph nodes in varying proportions but when selective ROIs were placed in relatively "pure" areas, we discovered that areas with tightly packed malignant cells tended to produce a slower MGE signal decay compared to desmoplastic or necrotic ones but still, the decay occurred much faster than in benign nodal tissue (Figure 5). To investigate the mechanism underlying the SPI decay differences, we performed staining for different markers (Figure 5). Importantly, no iron particle accumulation was found in the selected fields neither in benign nor in malignant nodes, suggesting iron is not involved in the contrasts obtained in this study.

3.3 Translation of SPI to the clinic, in-vivo at 1.5 T

We next aimed to assess the clinical applicability of SPI for mesorectal lymph node characterization prospectively, upon rectal cancer staging. The non-monoexponential nature of the MGE signal decay was evidenced for both benign (n = 36) and malignant (n = 27) lymph node datasets (63 lymph nodes in total), and again revealed radically different decay characteristics: the benign nodes had a much slower decay compared to the malignant. Figure 6 shows SPI decays from a benign and a malignant node and in Figure 1 from Supplementary Material, the corresponding full extent of TEs is displayed.

The BIC analysis ranked the biexponential model first and the monoexponential model last in most instances. Differences in the parameter values derived from the biexponential model are presented in Figure 7a. T_2*a carried differences between benign and malignant lymph nodes with statistical significance (malignant: median = 50.86 ms; iqr = 20.84 ms; benign: median = 58.87 ms; iqr = 29.50 ms; p = 0.02), as did T_2*b (malignant: median = 2.96 ms; iqr = 0.73 ms; benign: median = 3.59 ms; iqr = 6.17 ms; $p = 3x10^{-3}$). Both T_2*a and T_2*b were shorter in malignant lymph nodes, in accordance with the ex-vivo data. For a cutoff of 58.5 ms, T_2*a presented with an AuROC of 0.70 and for a cutoff of 53.2, T_2*b presented with an AuROC of 0.76. The combination of T_2*a+T_2*b resulted in an AuROC of 0.79 (Figure 7b). The performance of these metrics was superior to both that of T_2* derived from the monoexponential model (0.64) and that of the T_2-WI-based analysis (0.67 and 0.69 for the two radiologists observing the data, ICC = 0.70, considered good). Adding the T_2*a+b SPI analysis to the T_2-WI assessment increased the AuROC from 0.65 to 0.80 for Reader 1 and from 0.66 to 0.87 for Reader 2 (Figure 7c). The observed increase was statistically significant ($p = 8.6x10^{-4}$ and $p = 3x10^{-4}$ for Readers 1 and 2, respectively). However, the performance of the combination was not significantly improved when compared to the plain T_2*a+b SPI analysis (p = 0.90 and p = 0.26 for Readers 1 and 2, respectively).

4. DISCUSSION

Lymph node staging is crucial for clinical decision-making in the great majority of malignancies. In the particular case of rectal cancer, lymph node involvement before surgery is considered an indication for neoadjuvant therapy (18) but lymph node classification is limited based on standard imaging, namely high-resolution T_2-weighted MRI (4,5). Lymph node characterization can be improved using non-targeted imaging agent methods such as MR lymphography with USPIO nanoparticles which have been applied with very high accuracy (19,20,21) and AuROC above 0.90 (22,23). Very good results have also been reported using Gadofosveset, a gadolinium-based intravascular contrast agent (AuROC curve of 0.96) (24). The drawback of these techniques is that they involve the administration of exogenous contrast agents with their implicit adverse reactions. Moreover, these contrast agents are not available for clinical use, making these techniques impractical.

In this study, we hypothesized that the microstructural changes associated with tumor infiltration – namely, the presence of malignant epithelial cells, much larger and more densely packed than native leucocytes – would cause susceptibility-induced magnetic field perturbations that could be picked up using SPI – an MGE sequence acquired up to very long echo times. Our histology-inspired numerical simulations clearly revealed that the hypothesis is viable and that MGE signal decays non-exponentially with potentially oscillating features. We then applied SPI at ultrahigh field 16.4 T MRI to perform a “virtual histology” with sufficient resolution to actually resolve infiltrated regions vs. normal node tissue. Our experimental findings further corroborated our hypothesis: the SPI decays in the 64 lymph nodes dissected from the total mesorectal excision specimens of rectal cancer patients were dramatically different in benign and malignant tissue, both with respect to the phenomenological signal decay, which was slower for normal nodes, but also quantitatively, from the ensuing extracted parameters. Interestingly, we found 3 different types of malignant infiltration into the lymph nodes. Patterns included clumps of adenocarcinoma cells tightly packed together, areas of desmoplastic reaction and areas of necrosis/cystic degeneration. These patterns tend to coexist in varying proportions within and across lymph nodes but we were able to show – albeit qualitatively only – that the 3 different kinds of infiltration may be characterized by different SPI curves. While the prognostic impact of these histologic divergences is unknown, it may be worth exploring in the future to further assist in the decision-making framework.

To simplify the SPI analysis, we assumed that a small number of components could be fit to the data. T_2*b (the component with longer relaxation time) evidenced the most significantly different values and was much shorter in tumor tissue, though T_2*a was also significantly shorter. In absolute value, the frequency shift ($\Delta\Omega$) in tumor was higher, which is in line with the shorter relaxation rates observed.

The final step in the ex-vivo part of the study was corroborating the working hypothesis using histology. Our histology quantification data indicated that microstructural features, namely cellularity and cell size, influenced the extracted SPI parameters. Judging by Pearl's coloration, which was negative in both benign and malignant nodes studied, iron particle accumulation does not appear to be the source for the observed differences in the signal decays. Importantly, the shortening of both T_2* components observed in tumor ex-vivo were also evidenced in malignant nodes in-vivo. This suggests that oxygenation state, flow effects or tissue preparation are unlikely explanations for our results. All these lend further credence to our hypothesis: the microstructure itself induces the capability of differentiating between infiltrated and benign node tissue.

It could be argued that these results, that were obtained at such high magnetic fields, would not necessarily be translatable to the lower magnetic fields existing in clinical settings. However, although it could be expected that the field distribution strongly depends on the strength of the magnetic field, it is worth noting that the MGE phase, which governs the non-monoexponential decay observed above, goes as $\varphi_{MGE} = \gamma \Delta B \cdot TE$, which suggests that the lower ΔB can be compensated for with higher TE, and still obtain the same phase. We therefore translated the experiment to the clinical setting and scanned 63 mesorectal lymph nodes in rectal cancer patients both with SPI and the contemporary state-of-the-art high resolution T_2-WI evaluated by 2 expert radiologists according to current guidelines (17). We found that, in accordance with the ex-vivo experiment, the MGE signal is non-monoexponential and, in some cases, also nonmonotonic, and it was best characterized by a biexponential model. We further found that in most instances, T_2*a and T_2*b values were significantly lower in malignant lymph nodes. The differences were somewhat less pronounced than in the ex-vivo experiment, which may be justified by the smaller field strength and by the use of whole-node ROIs, required due to the constraints in clinical image resolution. Still, SPI parameters performed better than visual assessment by expert radiologists, with a higher sensitivity and no loss in specificity. We were therefore able to show that the simple SPI experiment provides indeed information on the microstructure also in-vivo and adds value to current standard evaluation based on T2-WI. Even though results were slightly inferior to those reported for USPIO and Gadofosveset enhanced MR imaging, unlike the latter, SPI is a simple, readily available and adverse-effect-free method that can easily complement T_2-WI during staging pelvic MRI of patients. It should be noted that SPI is expected to have a better performance at 3T or even higher fields that may become more clinically-relevant in the future. The separability of the curves is expected to be enhanced with increasing field, as the T_2*s shorten and the phase shifts increase due to stronger susceptibility perturbation (25-27). Moreover, an increase in SNR could facilitate higher resolution for characterizing smaller nodes.

This study of course also had several limitations. First, no lymph node tissue could be retrieved from very small lymph nodes (<3 mm), which biased our sample for larger nodes in both in-vivo and ex-vivo experiments. Second, a large heterogeneity in the signal intensity decay patterns of malignant datasets was found. However, these reflected to some extent an inherent variability in tumor spreading patterns, which as previously stated is hypothesized to carry relevant prognostic information. Third, the numerical simulations were somewhat simplified: the two tissue types assumed ideally spherical cells and that susceptibility does not vary between substrates. Additionally, when computing the MRI signal, diffusion effects were ignored, i.e., the static dephasing regime was assumed (12,13). Nevertheless, the simulated signal in this toy model showed similar trends to measured data, suggesting that differences in cellular size and packing density play an important role in the observed SPI contrast.

Finally, it is worth reflecting on the translation of these findings to other lymph nodes not necessarily originating from the mesorectum of rectal cancer patients. They might be particularly useful for urologic cancers such as prostate and bladder, for which high-mordibity-associated lateral pelvic lymph node dissection is still performed for staging purposes or based on indirect nomogram predictive model scoring rather than strictly to patients with lymph node involvement documented non-invasively (28,29).

5. CONCLUSION

SPI accurately characterizes lymph node tissue and improves specificity towards microstructural characterization. At least in part, the quantitative differences in the extracted parameters were explained by differences in cellularity and cell size between the tissues, as opposed to iron content or oxygenation state. Using the same methodology and without the need for exogenous contrast administration, we found concordant results in-vivo at 1.5T. When compared with expert visual assessment based on T_2-WI, SPI increased the accuracy of lymph node characterization upon clinical staging, with a significant improvement in sensitivity and no loss in specificity. It may therefore be of added value for patient selection for neoadjuvant therapy. The results given here are a first step that bodes well for future studies aiming to generalize SPI as a lymph-node specific biomarker.

ACKNOWLEDGEMENTS

The authors would like to thank the following for their contributions:

Lara Castanheira, Alexandra Ferreira and Ana Santos from the Pathology Department of the Champalimaud Centre for the Unknown;

Paula Montesinos and Javier Gonzalez-Sanchez from Philips Healthcare Iberia;

Nuno Figueiredo and José Filipe Cunha from the Digestive Unit of the Champalimaud Centre for the Unknown;

Carlos Leichsenring, Vasco Geraldes and Cisaltina Sobrinho, from the Department of Surgery of the Hospital Fernando Fonseca, EPE;

Maria Lisitskaya, a fellow radiologist at the Computational Clinical Imaging Group, Champalimaud Centre for the Unknown;

Nickolas Papanikolaou from the Computational Clinical Imaging Group, Champalimaud Centre for the Unknown;

All the staff from the Radiology Department of the Champalimaud Centre for the Unknown;

The researchers from the Neuroplasticity and Neural Activity MRI Lab, Champalimaud Centre for the Unknown.

FUNDING

This study was funded by the Champalimaud Centre for the Unknown.

Andrada Ianus´s work was supported by EPSRC grants EP/M020533/1 and EP/N018702/1

REFERENCES

1) Yao Y-F, Wang L, Liu Y-Q, Li J-Y and Gu J. Lymph node distribution and pattern of metastases in the mesorectum following total mesorectal excision using the modified fat clearing technique. 2011. J Clin Pathol. 64(12):1073-7.

2) Sauer R, Becker H, Hohenberger W, Rodel C, Wittekind C, Fietkau R, Martus P et al. Preoperative versus postoperative chemoradiotherapy for rectal cancer. N Engl J Med 2004; 351:1731-1740.

3) Damadian R. Tumour detection by nuclear magnetic resonance. 1971. Science. 171(3976):1151-3.

4) Jhaveri K, Hosseini-Nik H. MRI of Rectal Cancer: An Overview and Update on Recent Advances. Am J Roentgenol 2015. 205(1):42-55.

5) Bipat S, Glas AS, Slors FJM, Zwinderman AH, Bossuyt PMM, Stoker J. Rectal Cancer: Local Staging and Assessment of Lymph Node Involvement with Endoluminal US, CT, and MR Imaging—A Meta-Analysis. 2004. Radiology. 232(3):773-83.

6) Chavhan GB, Babyn PS, Thomas B, Shroff M and Haacke EM. Principles, techniques, and applications of T2*-based MR imaging and its special applications. Radiographics. 2009; 29(5): 1433–1449.

7) Korteweg MA, Zwanenburge JJM, Hoogduin JM, van der Bosch AAJ, van Diest PJ, van Hillegersberg R, Eijkemans JC et al. Dissected sentinel lymph nodes of breast cancer patients: characterization with high-spatial-resolution 7-T MR imaging. Radiology. 2011. 261: 127-135.

8) Li C, Meng S, Yang X, Wang J and Hu J. The value of T2* in differentiation metastatic from benign axillary lymph nodes in patients with breast cancer – a preliminary in vivo study. PloS One. 2014. 9(1):e84038.

9) Chen WC. Foxley S. Miller KL. Detecting microstructural properties of white matter based on compartmentalization of magnetic susceptibility. 2013. NeuroImage. 70: 1-9.

10) Nunes D, Cruz TL, Jespersen SN, Shemesh N. Mapping axonal density and average diameter in white matter using non-monotonic time-dependent gradient-echo MRI. J Magn Reson. 2017. 277:117-130.

11) Qian Y, Williams A A, Chu C R and Boada F E. Multicomponent T2* mapping of knee cartilage: technical feasibility ex vivo. Magn Reson Med. 2010. 64:1427-1432.

12) Weisskoff R, Zuo CS, Boxerman JL, Rosen BR. Microscopic susceptibility variation and transverse relaxation: Theory and experiment. Magn Reson Med. 1994. 31(6):601-10.

13) Salomir R, de Senneville BD, Moonen CTW. A fast calculation method for magnetic field inhomogeneity due to an arbitrary distribution of bulk susceptibility. Magn Reson Eng. 2003. 19B(1):26-34.

14) Kashevskii BE, Kashevskii SB, Prokhorov IV, Aleksandrova EN, Istomin YuP. Magnetophoresis and the magnetic susceptibility of HeLa tumor cells. Biophysics. 2006, 51, (6):902–907

15) Veraart J, Novikov DS, Christiaens D, Ades-Aron B, Sijbers J, Fieremans E. Denoising of diffusion MRI using random matrix theory. Neuroimage. 2016 Nov 15;142:394-406.

16) Kasper Marstal, Floris Berendsen, Marius Staring and Stefan Klein, "SimpleElastix: A user-friendly, multi-lingual library for medical image registration", International Workshop on Biomedical Image Registration (WBIR), Las Vegas, Nevada, USA, 2016

17) Beets-Tan RGH, Lambregts DMJ, Maas M, Bipat S, Barbaro B, Curvo-Semedo L et al. Magnetic resonance imaging for clinical management of rectal cancer: Updated recommendations from the 2016 European Society of Gastrointestinal and Abdominal Radiology (ESGAR) consensus meeting. 2018. Eur Radiol. 28(4):1465-1475

18) Benson AB, Venook AP, Al-Hawary MM, Cederquist L, Chen Y-J, Ciombor KK, Cohen S et al. Rectal Cancer, Version 2.2018, NCCN Clinical Practice Guidelines in Oncology. J Natl Compr Cnc Netw. 2018. 16:874-901.

19) Koh D-M, Brown G, Collins DJ. Nanoparticles in rectal cancer imaging. 2009. Cancer Biomarkers. 5: 89–98.

21

20) Wu L, Cao Y, Liao C, Huang J, Gao F. Diagnostic performance of USPIO-enhanced MRI for lymph-node metastases in different body regions: a meta-analysis. Eur J Radiol. 2011 Nov;80(2):582-9.

21) Torabi M, Aquino SL, Harisinghani MG. Current concepts in lymph node imaging. J Nucl Med. 2004; 45:1509-1518.

22) A.G. Rockall, S.A. Sohaib, M.G. Harisinghani et al., Diagnostic performance of nanoparticle-enhanced magnetic resonance imaging in the diagnosis of lymph node metastases in patients with endometrial and cervical cancer, J Clin Oncol 23 (2005), 2813–2821.

23) R. Sigal, T. Vogl, J. Casselman et al., Lymph node metastases from head and neck squamous cell carcinoma: MR imaging with ultrasmall superparamagnetic iron oxide particles (Sinerem MR) – results of a phase-III multicenter clinical trial, Eur Radiol 12 (2002), 1104–1113.

24) Lambregts DM, Beets GL, Maas M, et al. Accuracy of gadofosveset-enhanced MRI for nodal staging and restaging in rectal cancer. Ann Surg 2011; 253:539–45.

25) Kiselev VG,. Larmor frequency in heterogeneous media. J Magn Reson. 2019. 299:168-175.

26) He X, Yablonskiy DA, Biophysical mechanisms of phase contrast in gradient echo MRI. Proc. Nat. Acad. Sci. U.S.A. 2009 106(32):13558-63.

27) Sati P, van Gelderen P, Silva AC, Reich DS, Merkle H, de Zwart JA, Duyn JH. Micro-compartment specific T2∗ relaxation in the brain. NeuroImage 77 (2013) 268–278.

28) Porpiglia F, Manfredi M, Mele F, Bertolo R, Bollito E, Gned D, De Pascale A et al. Indication to pelvic lymph nodes dissection for prostate cancer: the role of multiparametric magnetic resonance imaging when the risk of lymph nodes invasion according to Briganti updated nomogram is <5. Prostate Cancer Prostatic Dis. 2018. 21(1):85-91.

29) Sundi D, Svatek RS, Nielsen ME, Schoenberg MP, Bivalacqua TJ. Extent of Pelvic Lymph Node Dissection During Radical Cystectomy: Is Bigger Better? Rev Urol. 2014; 16(4): 159–166.

FIGURE LEGENDS

Figure 1. Spatial distribution of the magnetic field induced by a distribution of spherical cells corresponding to a) benign tissue over a 50x50 μm^2 field of view in the XY and XZ planes and b) malignant tissue over a 50x50 μm^2 field of view in the XY and XZ planes. c) Normalised signal decay as a function of echo time for the two substrates corresponding to benign and malignant tissue. d) Normalised log signal decay as a function of echo time for the same two substrates.

Figure 2. a) Normalised average signal and log average signal with increasing TE of benign (n = 29) and malignant (n = 35) lymph node datasets. Shaded areas represent the standard deviation limits. **b)** Number of entries per rank of voxel-by-voxel analysis using Bayesian Information Criteria (BIC) for benign and malignant lymph nodes. Notice 2-compartment model ranked first and 1-compartment model ranked last in most instances for both benign and malignant datasets.

Figure 3. Boxplots depicting the measurement differences for the 2-compartment model-derived parameters Significant differences between benign and malignant lymph nodes were found for T_2*a, T_2*b and ΔΩ, but not for f.

Figure 4. a) T_2*b parametric maps and corresponding QuPath® cell detection tool applications are exemplified for a benign (above) and a malignant lymph node (below). **b)** Cellularity and cell size differences between benign and malignant lymph nodes are depicted in the boxplot above and Spearman correlations between them and T_2*b are depicted in the scatterplot below ($\rho = 0.52$ for cells/μm^2 and $\rho = -0.56$ for nuclear area, both considered moderate and both with $p < 0.01$).

Figure 5. When selective ROIs were defined, clear variations in SPI decay behavior are present. Highly cellular areas in secondary follicles from benign nodal tissue show a slower initial decline, whereas in tumor tissue, this decline tends to occur much faster and a clear oscillation between 20 and 40 ms becomes apparent. Pearls coloration was negative in all selected fields (iron particles stain in dark blue using Pearls coloration). CD45 is expressed in the cellular membrane of all leucocytes and benign lymph node tissue stains heavily, as expected. CK AE1/AE3 is a cytokeratin combination expressed in epithelial cells, including malignancies of epithelial origin such as colorectal adenocarcinoma. Although all malignant lymph node areas were positive, the area of high cellularity shows more pronounced staining and the corresponding early decay slope is higher when compared to other malignant patterns.

Figure 6. Examples of a benign and malignant lymph node as depicted in multiplanar high-resolution T_2-WI and MGE clinical images with increasing TE (only 9 TEs were depicted for simplicity but the full range of TEs is presented in Figure 1 from Supplementary material). A clearly faster loss of signal intensity with increasing TE is observed in the malignant lymph node. The corresponding single-slice whole-node ROI based decay curves again show non-monoexponential behavior.

Figure 7. a) Boxplots depict the significant differences in 2-compartment model-derived parameter values from the clinical dataset. **b)** ROC curves for monoexponential T_2* and biexponential T_2*a+b are also depicted, in which a clearly higher AuROC is present for the bi-compartmental model assessment. c) ROC curves for T_2-WI and T_2*a+b SPI analysis are shown, as well as their combination. The combination of the T_2-WI assessment with the SPI analysis performs best, showing the highest AuROC.

Figure 1

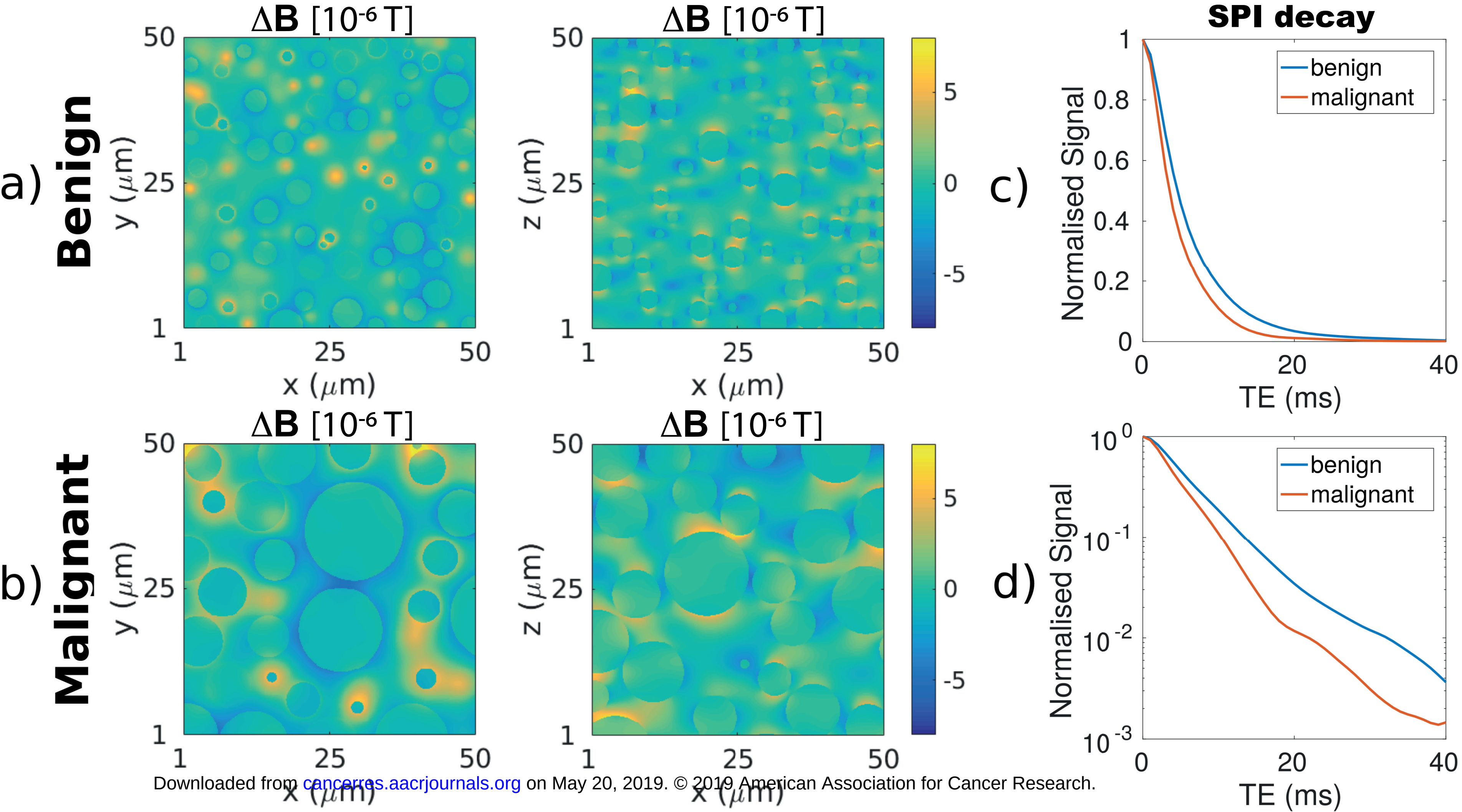

a)
Benign
ΔB [10^-6 T]
y (μm)
x (μm)
z (μm)
1
25
50
5
0
-5
b)
Malignant
c)
SPI decay
Normalised Signal
0
0.2
0.4
0.6
0.8
1
20
40
TE (ms)
benign
malignant
d)
10^0
10^-1
10^-2
10^-3

Figure 2

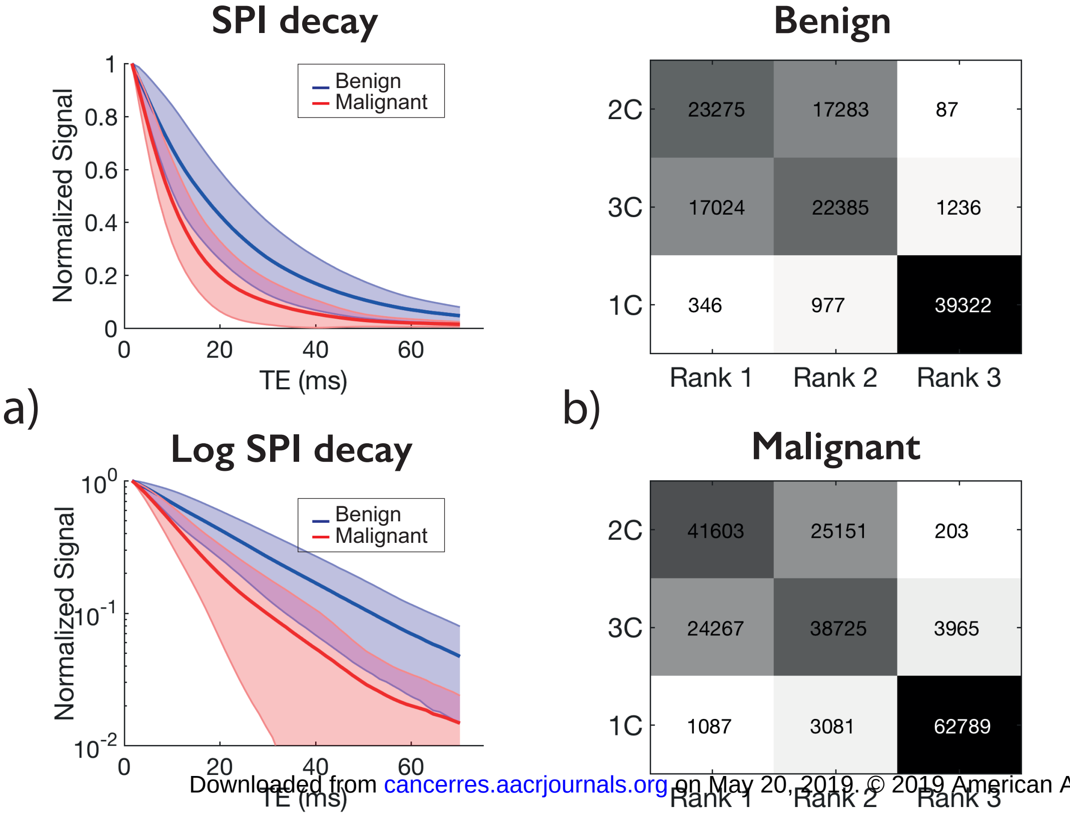

Benign

	Rank 1	Rank 2	Rank 3
2C	23275	17283	87
3C	17024	22385	1236
1C	346	977	39322

Malignant

	Rank 1	Rank 2	Rank 3
2C	41603	25151	203
3C	24267	38725	3965
1C	1087	3081	62789

Figure 3

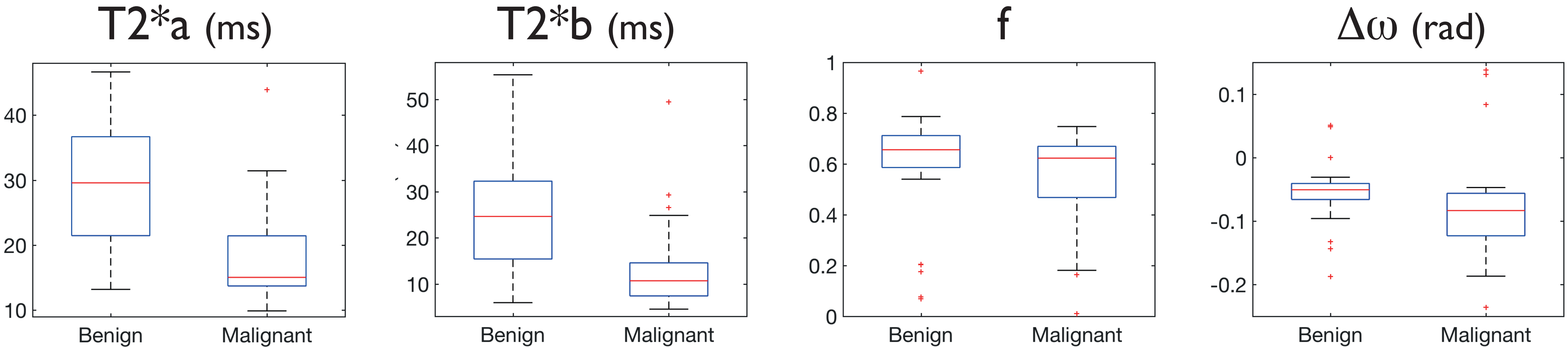
T2*a (ms)
40
30
20
10
Benign
Malignant
T2*b (ms)
50
40
30
20
10
Benign
Malignant
f
1
0.8
0.6
0.4
0.2
0
Benign
Malignant
Δω (rad)
0.1
0
-0.1
-0.2
Benign
Malignant

Figure 4

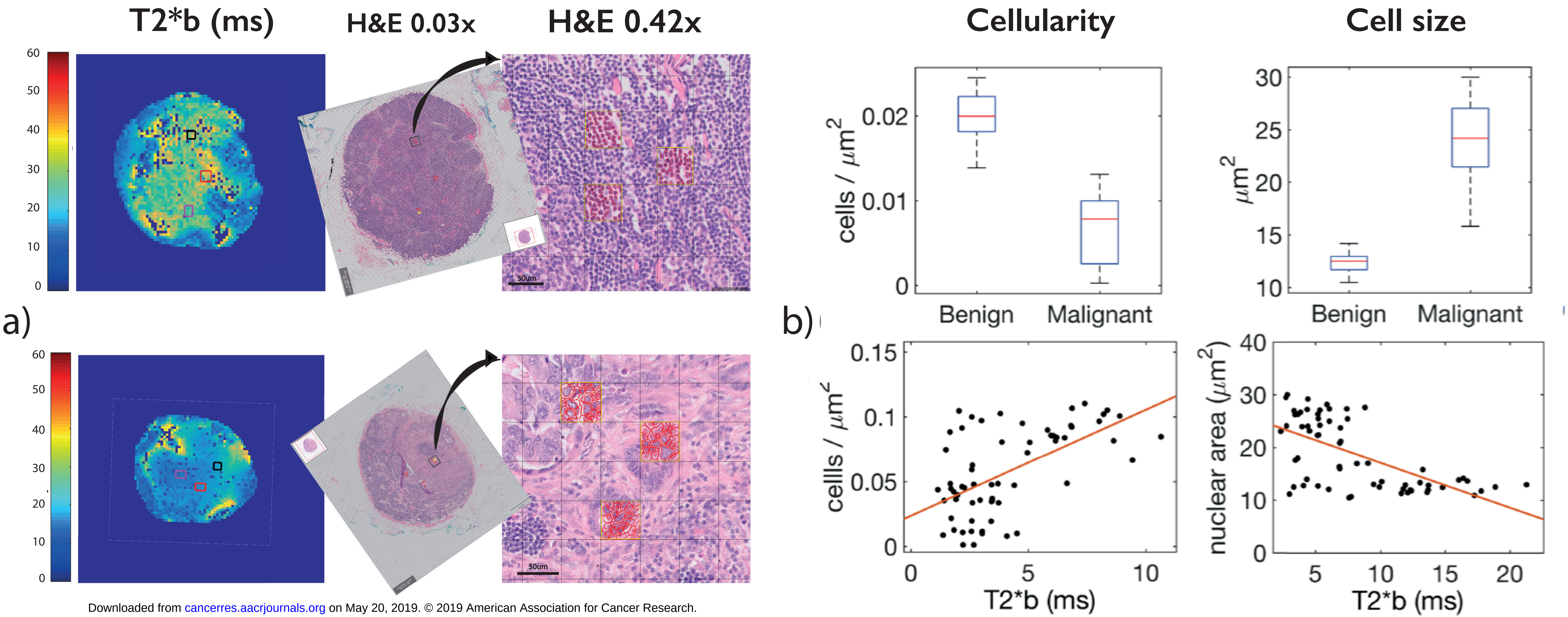
T2*b (ms)
H&E 0.03x
H&E 0.42x
Cellularity
Cell size
60
50
40
30
20
10
0
50um
a)
b)
cells / μm^2
0.02
0.01
0
Benign
Malignant
μm^2
30
25
20
15
10
Benign
Malignant
cells / μm^2
0.15
0.1
0.05
0
0
5
10
T2*b (ms)
nuclear area (μm^2)
40
30
20
10
0
5
10
15
20
T2*b (ms)

Figure 5

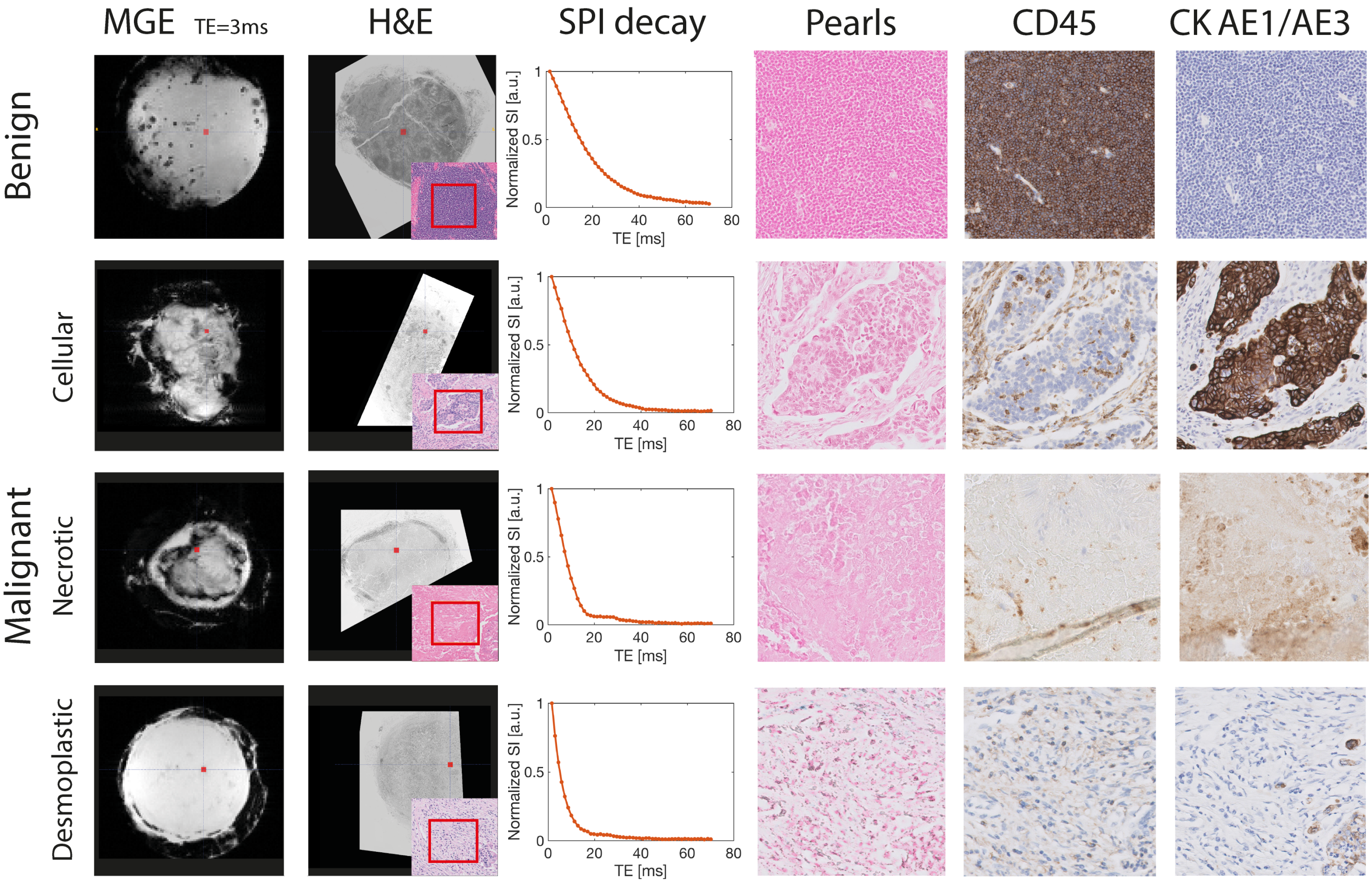
MGE TE=3ms
H&E
SPI decay
Pearls
CD45
CK AE1/AE3
Benign
Malignant
Cellular
Necrotic
Desmoplastic
Normalized SI [a.u.]
1
0.5
0
0
20
40
60
80
TE [ms]

Figure 6

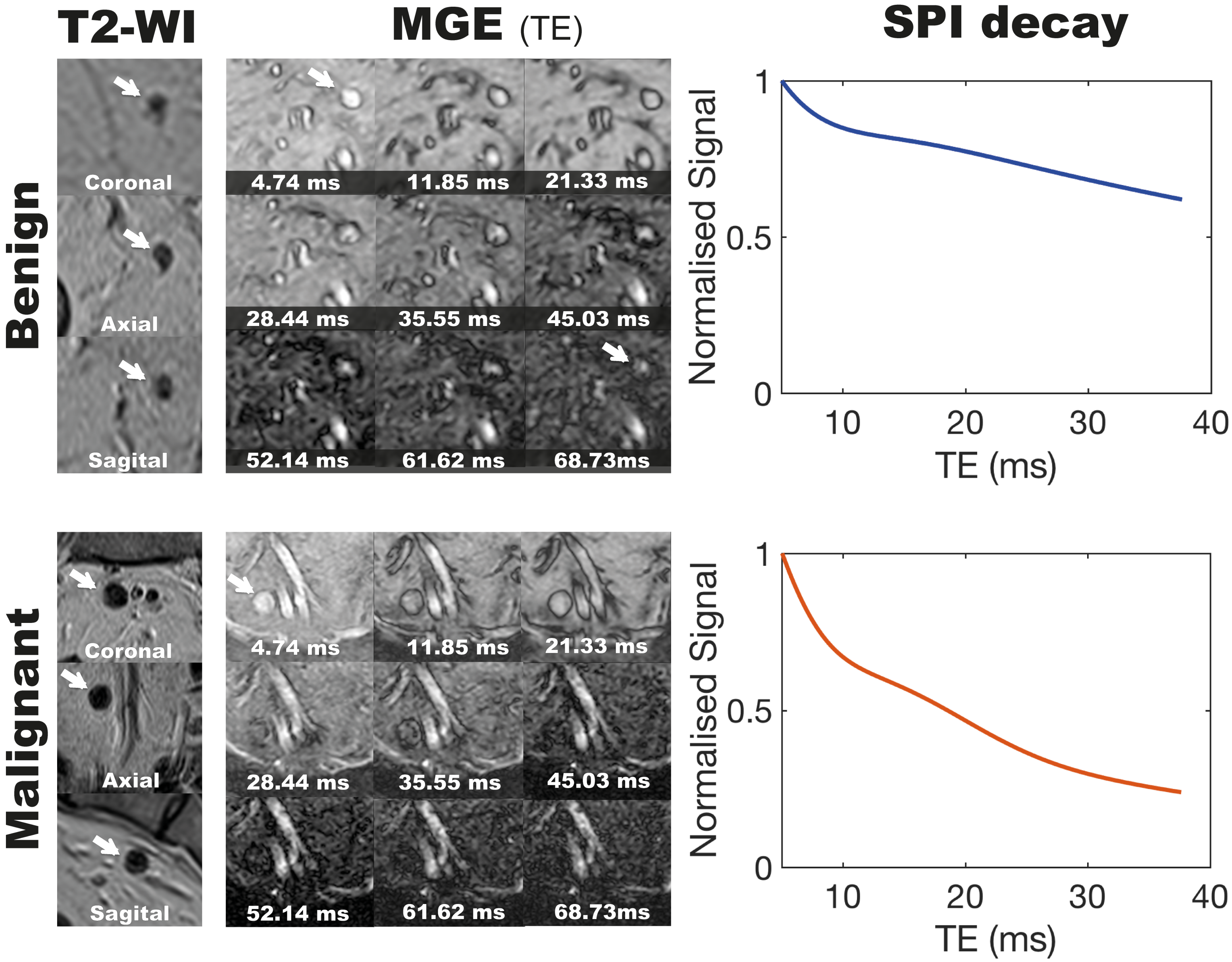
T2-WI
MGE (TE)
SPI decay
Benign
Coronal
Axial
Sagital
4.74 ms
11.85 ms
21.33 ms
28.44 ms
35.55 ms
45.03 ms
52.14 ms
61.62 ms
68.73ms
Normalised Signal
1
0.5
0
10
20
30
40
TE (ms)
Malignant
Coronal
Axial
Sagital
4.74 ms
11.85 ms
21.33 ms
28.44 ms
35.55 ms
45.03 ms
52.14 ms
61.62 ms
68.73ms
Normalised Signal
1
0.5
0
10
20
30
40
TE (ms)

Figure 7

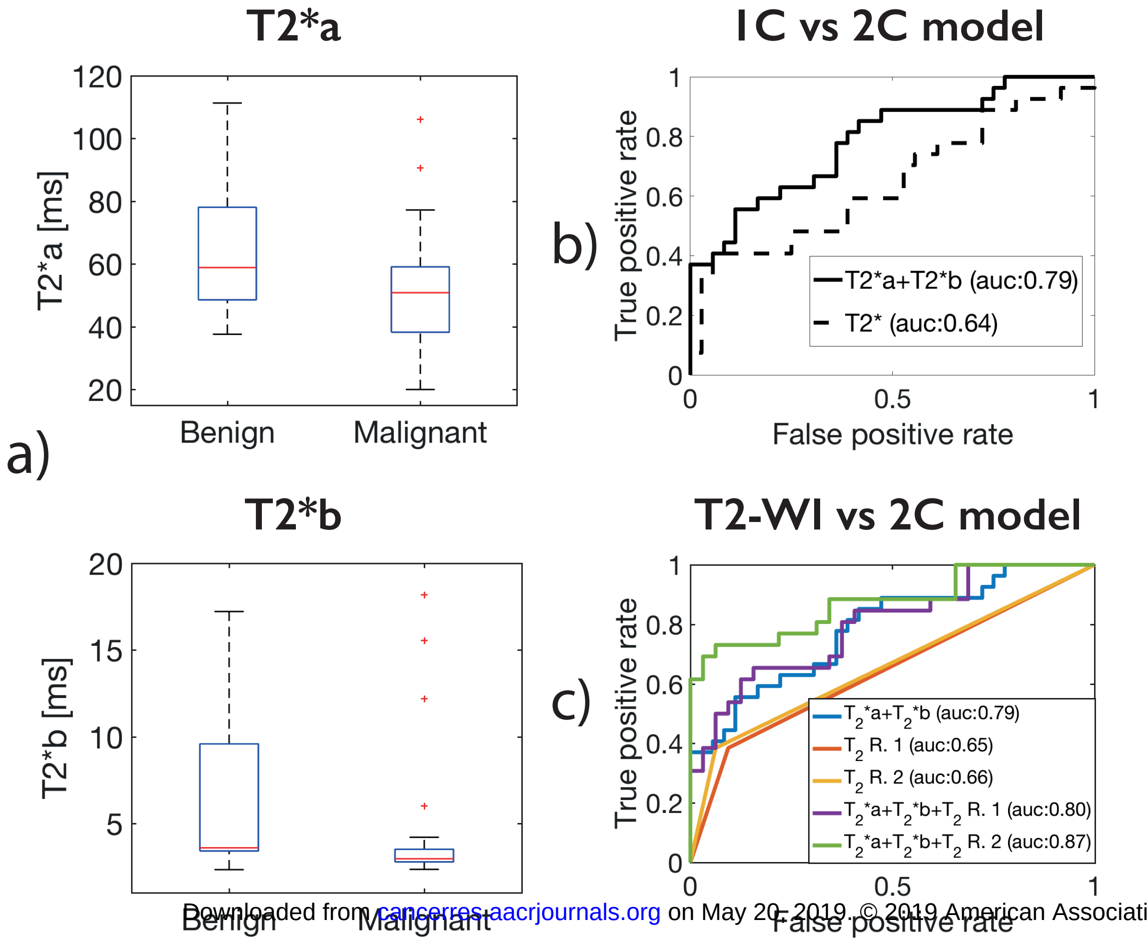
T2*a
120
100
80
60
40
20
T2*a [ms]
Benign
Malignant
a)
1C vs 2C model
1
0.8
0.6
0.4
0.2
0
True positive rate
0
0.5
1
False positive rate
b)
T2*a+T2*b (auc:0.79)
T2* (auc:0.64)
T2*b
20
15
10
5
T2*b [ms]
Benign
Malignant
T2-WI vs 2C model
1
0.8
0.6
0.4
0.2
0
True positive rate
0
0.5
1
False positive rate
c)
T_2*a+T_2*b (auc:0.79)
T_2 R. 1 (auc:0.65)
T_2 R. 2 (auc:0.66)
T_2*a+T_2*b+T_2 R. 1 (auc:0.80)
T_2*a+T_2*b+T_2 R. 2 (auc:0.87)

Cancer Research
The Journal of Cancer Research (1916–1930) | The American Journal of Cancer (1931–1940)

American Association for Cancer Research

Susceptibility perturbation MRI (SPI) maps tumor infiltration into mesorectal lymph nodes

Inês Santiago, João Santinha, Andrada Ianus, et al.

Cancer Res Published OnlineFirst March 20, 2019.